Supplementary Information

Large scale self-supported WP-W_2C nanoporous network for efficient hydrogen evolution reaction in alkaline media

Jingwen Huang[a], Chuanyong Jian[ab], Qian Cai[a], Wenting Hong[a]* and Wei Liu[ac]*

[a] CAS Key Laboratory of Design and Assembly of Functional Nanostructures, and Fujian Provincial Key Laboratory of Nanomaterials, Fujian Institute of Research on the Structure of Matter, Chinese Academy of Sciences, Fuzhou, Fujian, 350002, PR China

[b] University of Chinese Academy of Sciences, Beijing, 100049, China.

[c] Fujian Science & Technology Innovation Laboratory for Optoelectronic Information of China, Fuzhou, Fujian 350108, P. R. China.

E-mail: hongwenting@fjirsm.ac.cn; liuw@fjirsm.ac.cn

DFT Caculation

We have employed the first-principles by the Vienna ab initio simulation package[1,2] to perform all Spin-polarization density functional theory (DFT) calculations within the generalized gradient approximation (GGA) using the Perdew-Burke-Ernzerhof (PBE)[3] formulation. We have chosen the projected augmented wave (PAW) potentials[4, 5] to describe the ionic cores and take valence electrons into account using a plane wave basis set with a kinetic energy cutoff of 500 eV. Partial occupancies of the Kohn-Sham orbitals are allowed using the Gaussian smearing method and a width of 0.05 eV. The electronic energy is considered self-consistent when the energy change is smaller than 10^{-5} eV. A geometry optimization is considered convergent when the energy change is smaller than 0.04 eV $Å^{-1}$. The vacuum spacing in a direction perpendicular to the plane of the structure is 15 Å. The Brillouin zone integration is performed using 3×5×1 Monkhorst-Pack k-point sampling for a surface and interface structure.

Due to the nanoporous morphology of WP-W_2C that contains different facets, the crystal faces with the lowest surface energy are considered for the calculation. Although the crystal face with the lowest surface energy is not necessarily the one with the best activity, its crystal face has a higher probability of exposure. The surface energy is calculated using the equation: $\gamma=(E_{slab}-n*E_{bulk})/2A$, where E_{slab}, and E_{bulk} are the total energies of slab model, unit cell of bulk system. n is multiple of atomic number between slab model and bulk system. $2A$ presents the surface areas of two cleavage sides. Fig. S16 illustrates the surface energy of W_2C and WP with different

facets, W_2C (011) and WP (001) surfaces display the lowest surface energies, respectively. Therefore, these surfaces and their heterojunction are used to the DFT recalculations.

Finally, the adsorption energies (E_{ads}) are calculated as $E_{ads}= E_{ad/sub} -E_{ad} -E_{sub}$, where $E_{ad/sub}$, E_{ad}, and E_{sub} are the total energies of the optimized adsorbate/substrate system, the adsorbate in the structure, and the clean substrate, respectively. The free energy is calculated using the equation:

$$G = E + ZPE - TS$$

where *G, E, ZPE* and *TS* are the free energy, total energy from DFT calculations, zero point energy and entropic contributions, respectively.

Experimental section

Fabrication of WO_3/W

W foil is used as the substrate and is ultrasonic cleaning with acetone, ethanol, and distilled water for 10 minutes successively. The cleaned W foil is dried by Nitrogen gas (N_2, 99.99%) to remove the residual moisture. The oxidation of W foil is divided into two steps. Firstly, the dried W foil is calcined in the air at 600 °C for 2 hours in the tube furnace with a temperature rate of 10 °C min^{-1} to form a thin WO_2 layer on the surface of the W foil. Then the as-prepared WO_2/W film is cooled down to room temperature by natural air convection in the furnace. Secondly, the pre-treated WO_2/W film is placed on an alumina boat in the center of heating region. The tube furnace is setting in the mixed atmosphere of 20% oxygen and 80% argon in rough vacuum condition with the relative pressure range of -0.06 ~ -0.09 M pa. Then the

reaction is performed at the temperature of 800 °C with a warming-up time of 20 minutes and held the temperature for 40 minutes. It's important to note that the pressure of rough vacuum is too low to form the WO_3 layer, but too high to damage the WO_3 layer. In this way, a thin WO_3 layer can be formed on the W substrate and create the robust chemical bonds at the interface between WO_3 layer and W foil.

Preparation of WP/W

WP is grown by chemical vapor deposition synthesis using WO_3/W film and phosphorus powder (AR, 98.5%, 50 mg) as precursors. The WO_3/W film put on an alumina boat is placed in the center of heating region in a 2-inch diameter quartz-tube furnace. Another alumina boat with 50 mg P powder is loaded in the upstream zone (out of the heating scope) of the furnace. When the temperature of the heating zone reaches to 800 °C at the speed of 20 °C min^{-1}, the alumina boat of P powder is inlet into the heating scope of the tube furnace with a distance of 10 centimeters from WO_3/W film. The temperature is held for 20 minutes within the atmosphere of mixed gas (60 sccm Ar and 30 sccm H_2). After the phosphorization process, turn off CH_4 and H_2, the system cools down to the room temperature in an Ar gas flow of 30 sccm.

Preparation of W_xC/W

To prepare the W_xC/W sample, the WO_3/W film is heated up to 800 °C with a flowing mixture gas of H_2 and Ar (H_2/Ar=30:60) at a heating rate of 20 °C min^{-1}. Subsequently the methane (CH_4, 15 sccm) gas is inlet into the tube to make WO_3/W film undergo the carburization process when the tubular furnace reaches 800 °C and retains 20 minutes. After the carburization process, the CH_4 is turned off and W_xC/W

film cools down to the room temperature in an Ar gas flow of 30 sccm.

Preparation of WP-W_2C/W

The preparation process is the same as that of WP/W except that high purity methane gas (CH_4, flow of 15 sccm) is inlet along with the import of phosphorus powder when the temperature reaches 800 °C. The temperature is then held at 800 °C for 20 minutes.

Structural characterizations of the electrocatalyst.

The morphologies of the as-grown W foil, W_xC, WP and WP-W_2C samples are characterized by scanning electron microscopy (Zeiss FE-SEM Sigma300). X-ray diffraction (XRD) spectras are obtained using the D8 ADVANCE diffractometer with Cu Kα radiation (λ = 1.5418 Å). X-ray photoelectron spectroscopy (XPS) measurements are carried out by a ESCALAB 250Xi system (Thermo Fisher), equipped with a 100 W Al Kα source on a spot size of 100 μm at a 45° incident angle. The binding energy scan ranges from 0 to 1200 eV with an interval step of 1 eV, high-intensity excitation is provided by monochromatic Al Ka X-rays that are 1486.6 eV in energy with a 0.48 eV resolution at full width at half-maximum. The binding energy scale is calibrated to carbon line of 284.8 eV. All XPS spectras are recorded with a resolution of 50 meV. Each data set is first corrected for the nonlinear emission background. The data is then fitted with Gaussian function to find the deconvoluted peak positions. Transmission electron microscopy (TEM), high-resolution TEM (HRTEM), selected-area electron diffraction (SAED) and energy dispersive X-ray spectroscopy (EDS) mapping studies are conducted on a probe-corrected transmission

electron microscope operating at 200 kV (FEI Titan F20 TEM).

Contact angle

The water contact angle (CA) is measured at 25 ^{o}C in the air using the sessile drop technique with the following steps. Firstly, a 2-μl sessile droplet is deposited by a syringe pointed vertically down onto the sample surface. Then, a high-resolution camera captures the image, which will be analyzed by the image analysis software. Hence, the static contact angle is determined. For a sample surface, the static contact angle is the mean value of the static contact angles measured at twenty different points uniformly distributed on the surface (five measurements are made at each point). The uncertainty on such measurements is estimated to be ±5. Low values of the contact angle correspond to high surface wettability.

The relationship of contact angle and break-off diameter of the gas bubble can be described by the Fritz correlation:

$$D_{dp} = 0.20 \times \theta \times \left(\frac{\sigma}{g\left(\rho_l - \rho_g\right)} \right)^{0.5}$$

where D_{dp} refers to the bubble break-off diameter (m), θ is the contact angle (degree), σ refers to liquid-air surface tension (N/m), g refers to the acceleration due to gravity (m^2/s) and, ρ_l and ρ_g are the density of liquid (water) and gas (air) in units of kg/m^3, respectively. Thus, the diameters of bubbles are proportional to the contact angle at the same condition.

Table S1. Comparison of HER performance of WP-W_2C/W electrode with reported WP, WC or W_2C based electrocatalysts in 1.0 M KOH electrolyte.

Materials	η_{10} (mV)	η_{100} (mV)	Tafel slope (mV/dec)	Ref.
WP-W_2C/W	**43**	**139**	**42.11**	**This work**
p-WCx NWs/CC	122	204	56	Ref. 11
$Ni(OH)_2$-WP	77	-	71	Ref. 19
WP NPs@NC	150	-	34	Ref. 33
W_2C/CNT	148	290	56.2	Ref. S6
WP NAs/CC	150	271	102	Ref. 31
WP@NC	232	-	88	Ref. 35
WP_2 NSs/W	90	213	80.88	Ref. S7
W_2C/WP@NC	116.37	-	59.07	Ref. 14
W_2C@CNT	125	370	104	Ref. S8
W_2C	130	535	100	Ref. S9
W-W_2C/CNT-6	147	-	51	Ref. 15
WC/W_2C@C NWs	56	-	59	Ref. 10
P-W_2C@NC	63	-	-	Ref. 16
W_2C/C-20 NFs	81	137	53.5	Ref. 9
WC (WO_3)	68	-	38.9	Ref. 17
Twin WCN	138	-	-	Ref. 18

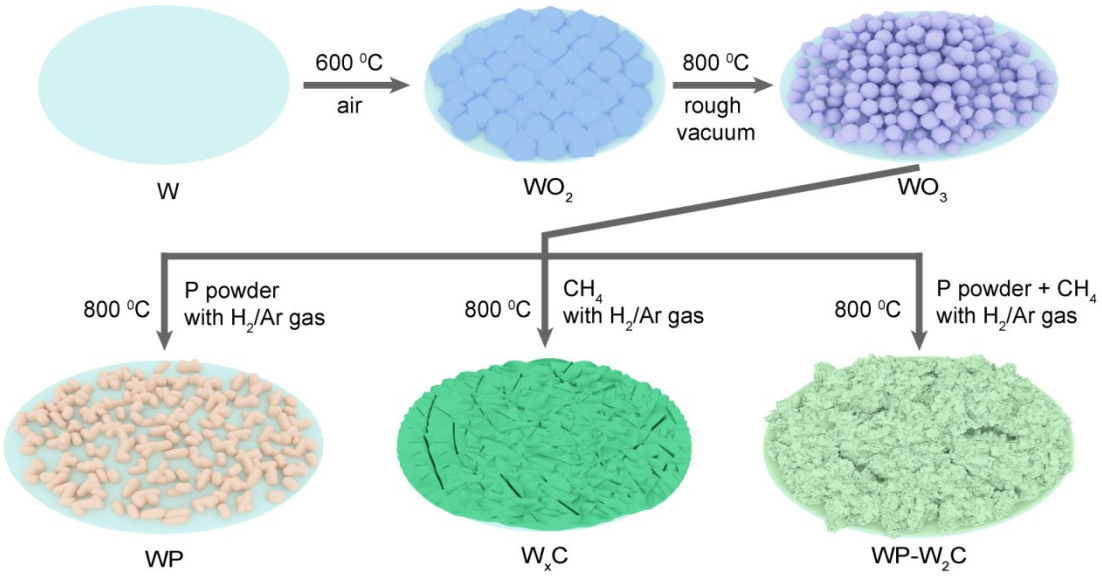

Fig. S1 Schematic illustration of the synthesis procedure of WP, W_xC and WP-W_2C on the W foil surface.

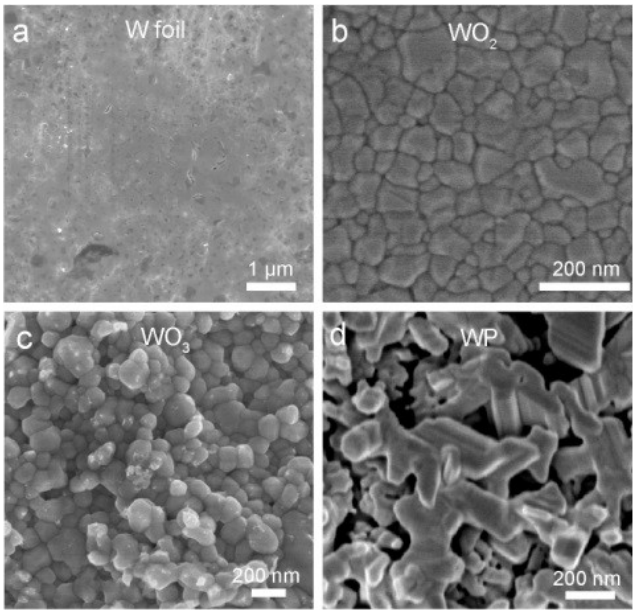

Fig. S2 SEM of (a) W foil, (b) WO_2, (c) WO_3, (d) WP catalysts with different magnifications.

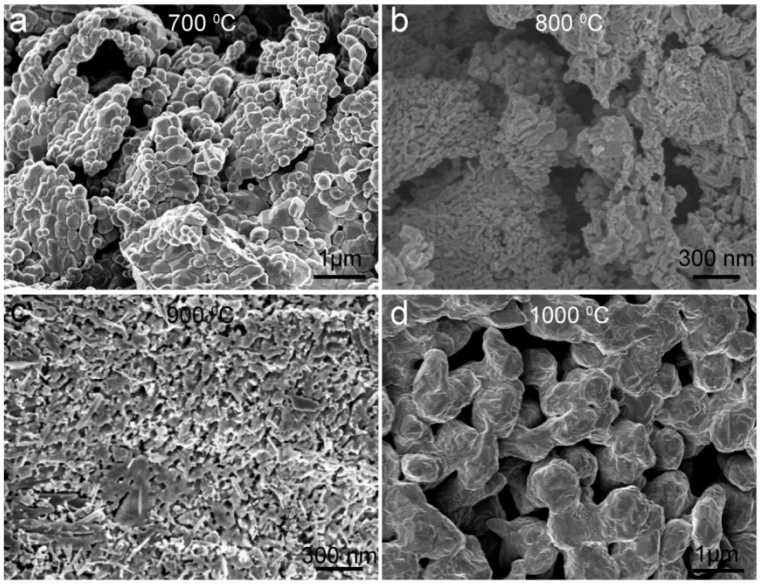

Fig. S3 SEM of WP-W_2C catalysts reacted with different temperatures of (a) 700 °C, (b) 800 °C, (c) 900 °C and (d) 1000 °C.

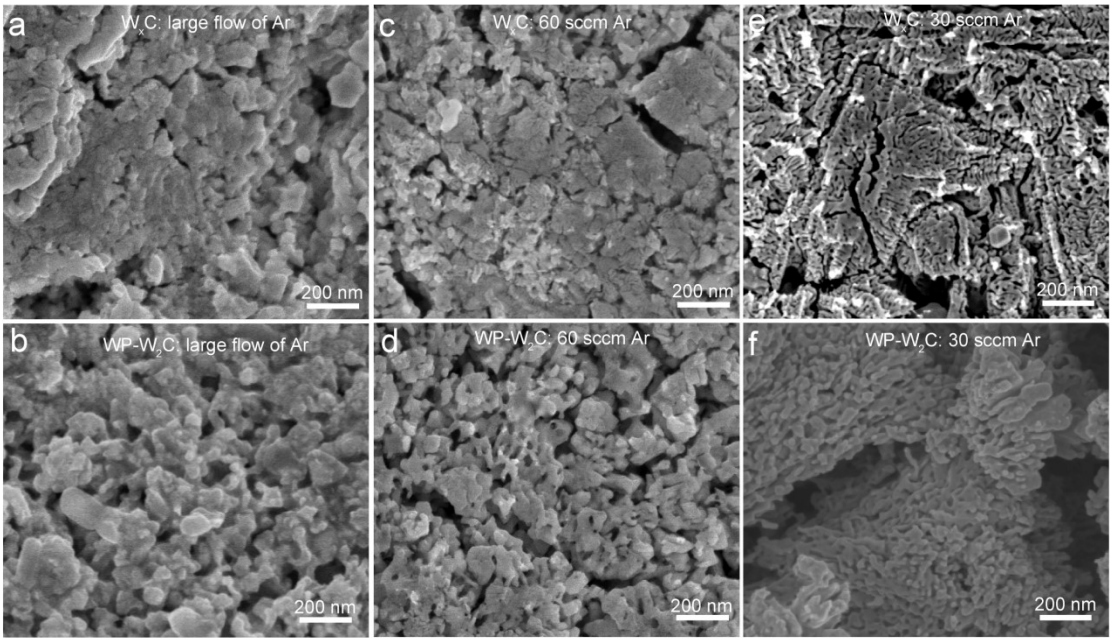

Fig. S4 SEM of W_xC and WP-W_2C catalysts with different gas flow rates of Ar during the cool down processes. It began to appear cracks on the surface of block W_xC with 60 sccm Ar, and there are nanoporous structures with 30 sccm Ar. The introduction of P precursor can appropriately increase the pores of nanoporous structure.

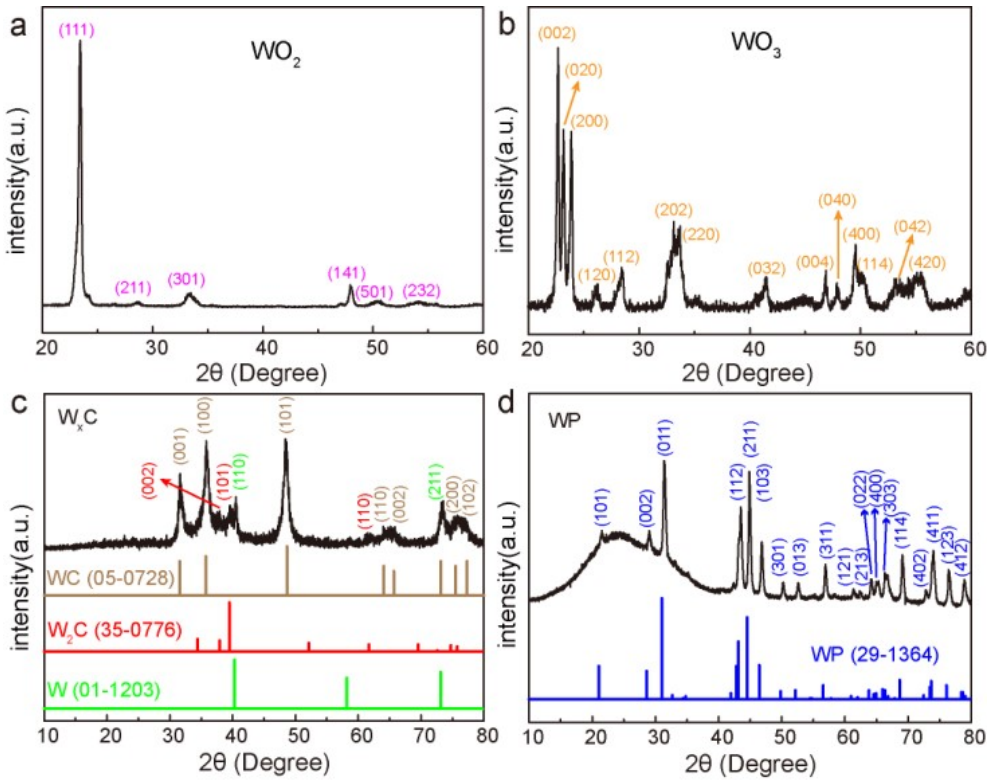

Fig. S5 XRD of (a) WO_2, (b) WO_3, (c) WC and (d) WP catalysts.

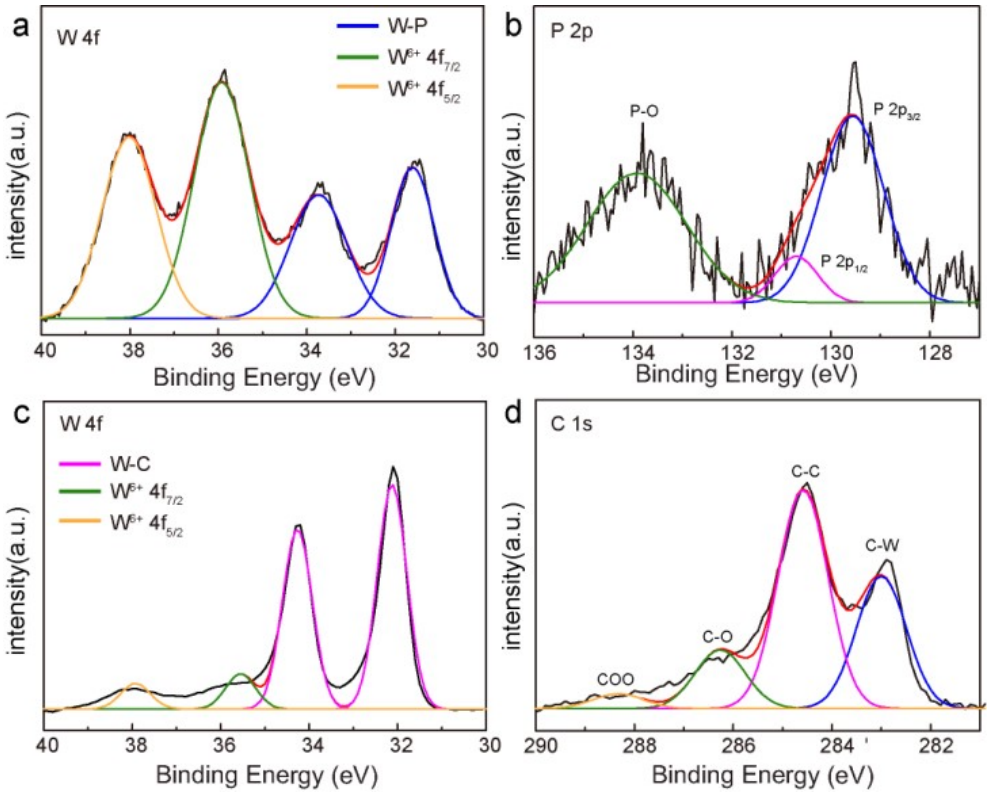

Fig. S6 X-ray photoelectron spectroscopy (XPS) spectra of (a) W 4f, (b) P 2p for WP and (c) W 4f, (d) C 1s for W_xC, respectively.

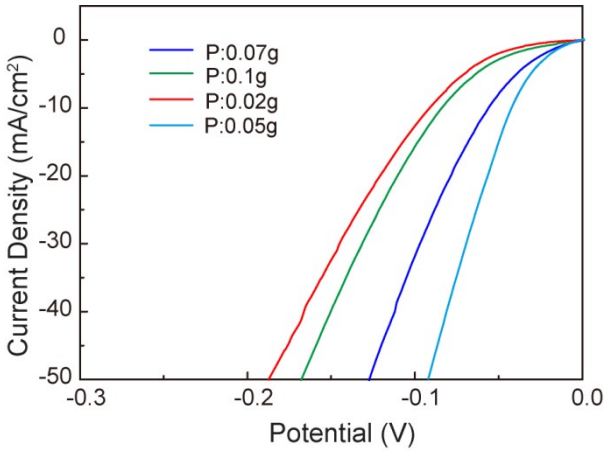

Fig. S7 Polarization curves of WP-W_2C catalysts with P power at different dosage measured in 1 M KOH solution.

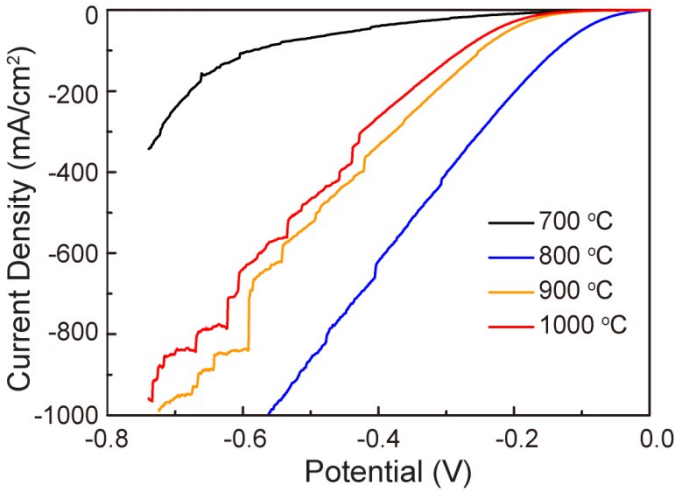

Fig. S8 Polarization curves of WP-W_2C catalysts with different temperatures measured in 1 M KOH solution.

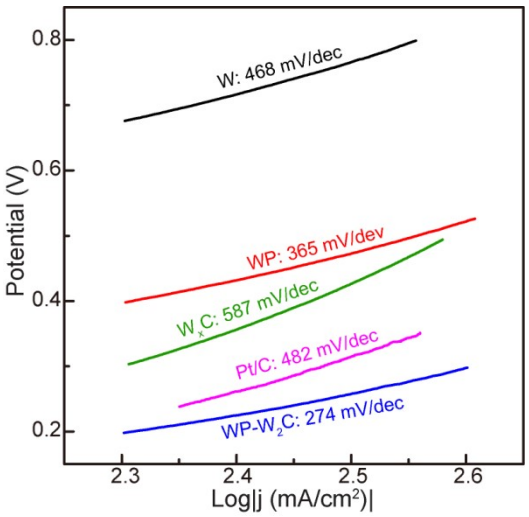

Fig. S9 Slope plots of different electrodes at the current density ranging from 200 to 500 mA/cm^2.

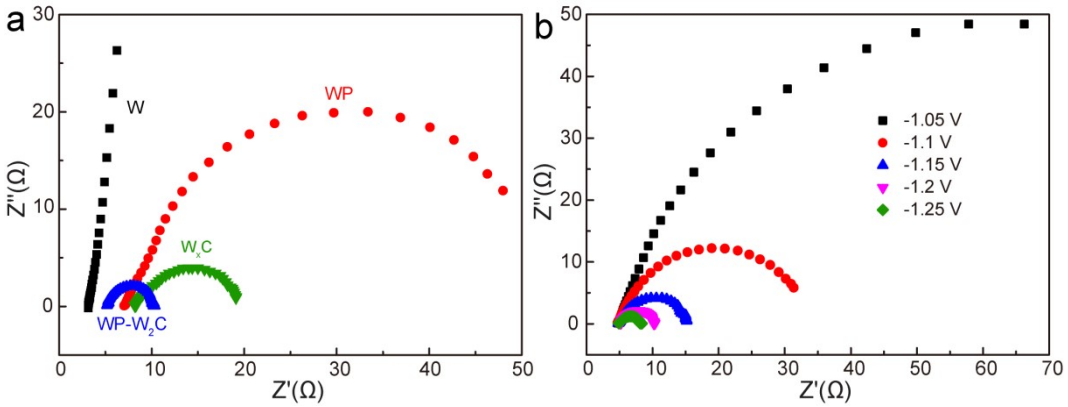

Fig. S10 (a) The Nyquist plots of different catalysts at potentials of -1.2 V in 1.0 M KOH electrolyte. (b) The Nyquist plots of WP-W_2C catalyst with different potentials.

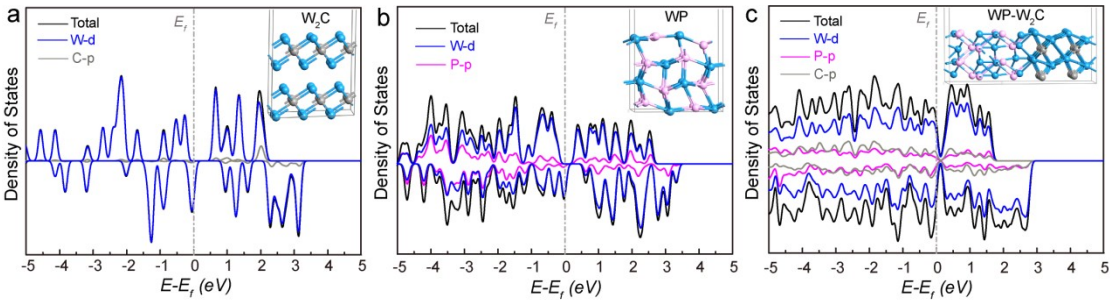

Fig. S11 Partial density of states and atom structures for (a) W_2C, (b) WP and (c) WP-W_2C.

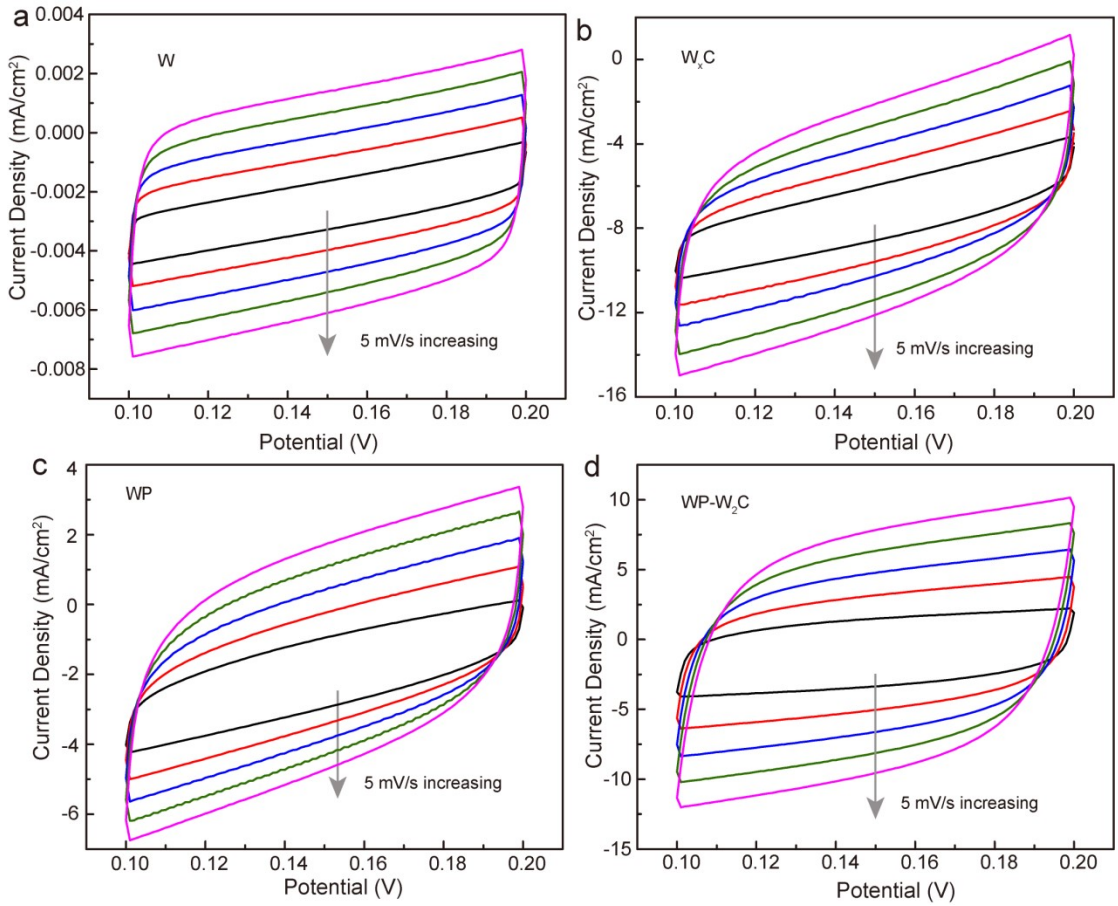

Fig. S12 The auxiliary cycle voltammetry (CV) tested with different scan rates of (a) W foil, (b) W_xC, (c) WP and (d) WP-W_2C catalysts in 1.0 M KOH.

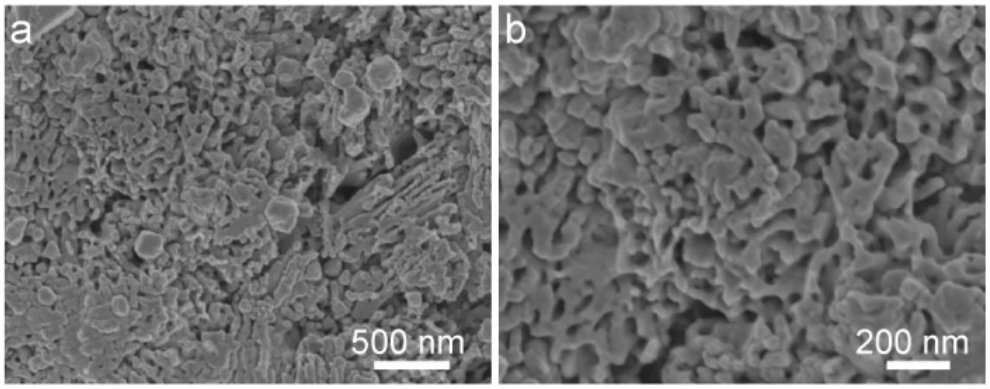

Fig. S13 SEM image of the WP-W_2C sample after the stability test. We found the rough surface and the decreased porosity of nanoporous WP-W_2C after stability test in alkaline media.

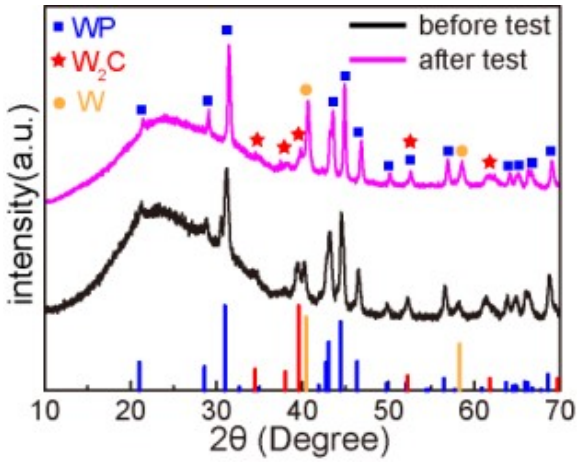

Fig. S14 XRD spectra of the WP-W_2C sample before and after the stability test. It can be observed that no obvious changes in the crystal structure before and after the stability test, indicating the WP-W_2C catalyst does not change in phase.

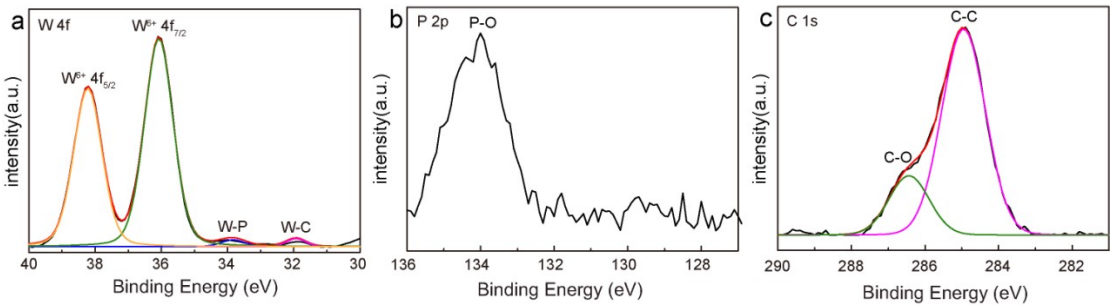

Fig. S15 XPS spectra of the WP-W_2C sample after the stability test. The W 4f core level can detect two intense bands at 36.0 and 38.3 eV, corresponding to the abundant surface hydroxyls and oxygen from oxides/hydroxides, the other weakened shoulders are W-C and W-P components. The single peak in the P 2p core level is ascribed to phosphate specie, the complete disappearance around the binding energy of 130 eV indicates the absence of phosphide components. The C 1s core level also exhibits the absence bands of C-W peak. These results suggest the further oxidation of catalyst after test in alkaline media. Presumably it's because the 5d metal tungsten is lack of electron with rich empty orbit, it has the strong OH* adsorption ability so that it is likely to lead to the advanced oxidation on the sites of tungsten.

Therefore, the catalyst is stable with WP and W_2C phase, but there are some changes in the morphology structure and valence state of W, P and C elements on the surface of catalyst. These changes in morphology and chemical state of elements may explain the degradation of HER activity after stability test.

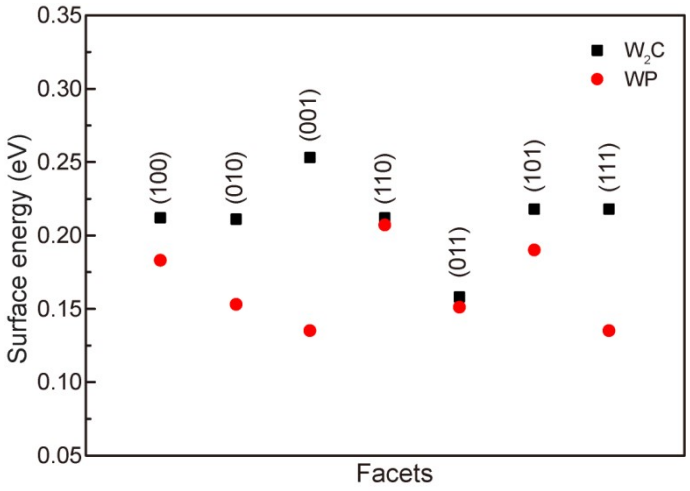

Fig. S16 the surface energy of W_2C and WP with different facets.

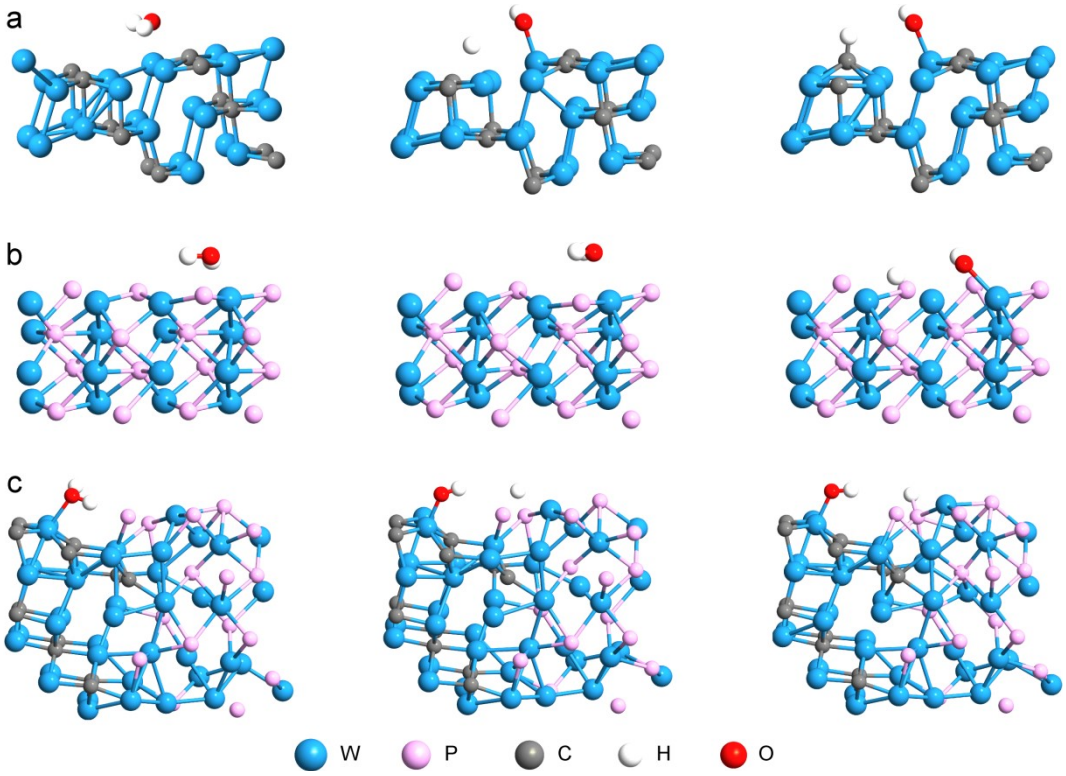

Fig. S17 Atomic structure diagram of initial, transition state and product for the water dissociation process for (a) W_2C (011) plane, (b) WP (001) plane, (c) WP (001)-W_2C (011) interface.

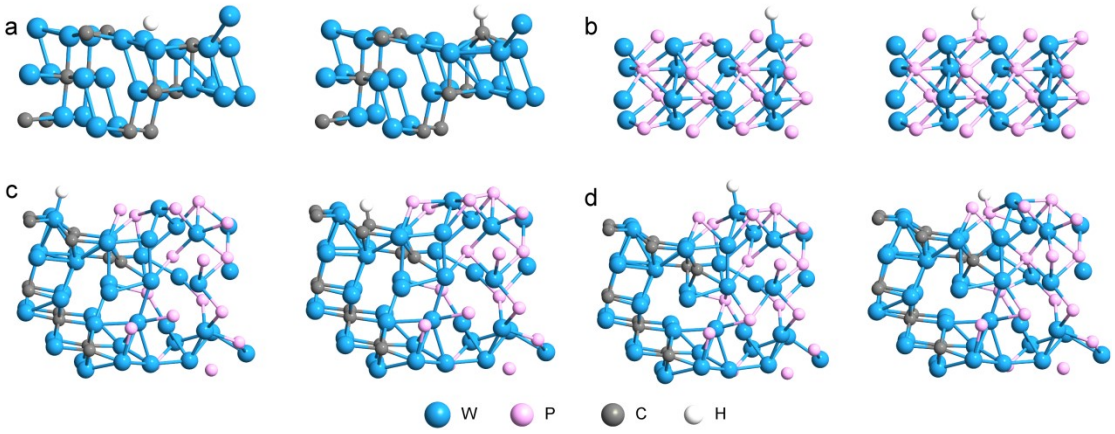

Fig. S18 Atomic structure diagram of H absorption on (a) W and C sites for W_2C (011) plane, (b) W and P sites for WP (001) plane, (c) W and C sites of W_2C for WP (001)-W_2C (011) , (d) W and P sites of WP for WP (001)-W_2C (011).

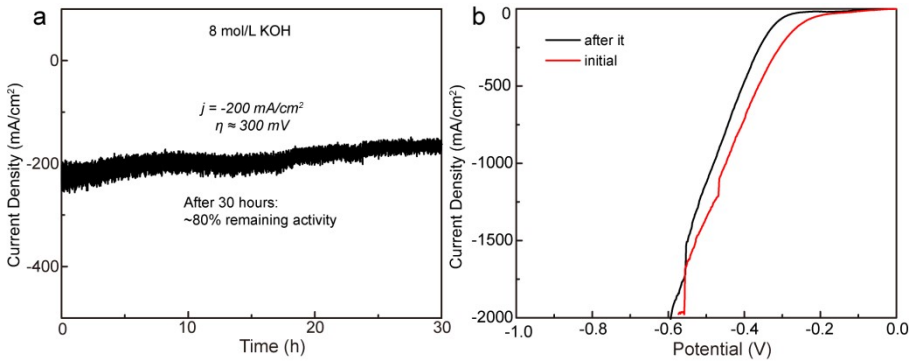

Fig. S19 The corrosion test of WP-W_2C catalyst in 8 mol/L KOH solution.

References

1. G. Kresse and J. Furthmüller, Comput. *Mater. Sci.*, 1996, **6,** 15-50.

2. G. Kresse and J. Furthmüller, *Phys. Rev. B*, 1996, **54**, 11169-11186.

3. J. P. Perdew, K. Burke and M. Ernzerhof, *Phys. Rev. Lett.*, 1996, **77**, 3865-3868.

4. G. Kresse and D. Joubert, *Phys. Rev. B*, 1999, **59**, 1758-1775.

5. P. E. Blöchl, *Phys. Rev. B*, 1994, **50**, 17953-17979.

6. Y. Hu, B. Yu, W. Li, M. Ramadoss and Y. Chen, *Nanoscale*, 2019, **11**, 4876-4884.

7. Q. Qin, J. Li, Z. Guo, C. Jian and W. Liu, *Int. J. Hydrogen Energ.*, 2019, **44**, 27483-27491.

8. S. Hussain, I. Rabani, D. Vikraman, A. Feroze, K. Karuppasamy, Z. Haq, Y.-S. Seo, S.-H. Chun, H.-S. Kim and J. Jung, *ACS Sustainable Chem. Eng.*, 2020, **8**, 12248-12259.

9. S. Hussain, D. Vikraman, A. Feroze, W. Song, K.-S. An, H.-S. Kim, S.-H. Chun and J. Jung, *Front. Chem.*, 2019, **7**.